Cable-Driven Continuum Robot Perception Using Skin-Like Hydrogel Sensors

Huizhen Yan, Yi Wang, Wenjun Shen, Famin Li, Guorong Gao,* Tianjiang Zheng,* Zhenyu Xu, Shuwen Qian, Chin-yin Chen, Chi Zhang,* Guilin Yang, and Tao Chen*

The cable-driven continuum robot (CDCR) is a highly significant soft robot that exhibits a lightweight structure, intrinsic safety properties, and a considerable degree of freedom; therefore, it can work well in confined and complex environments. However, commonly used fiber Bragg grating sensors in CDCR systems are ultra-stiff, extremely low in elongation, and lack an adhesion mechanism; this significantly restricts the movement of the robot and tends to delaminate from it, which makes it unsuitable for integrated systems. In this study, a new strategy is developed to enable CDCR perception via skin-like hydrogel sensors made from ionic conductive polyacrylamide/alginate/ nanoclay polymeric composite hydrogels; it exhibits a fracture strain of 1840% and adheres to a CDCR backbone with an adhesion strength of 6.6 kPa. The sensors are sensitive, stable, and reliable, and they can be manually operated to draw portraits using sensing curves as painted lines. Through these sensors, the CDCR acquires proprioception for sensing movements and exteroception for sensing barriers and traps. The hydrogel sensors are further employed to build a closed-loop control system for regulating the bending of the CDCR. This study establishes effective routes for designing sensors and closed-loop systems that can be applied to soft robots.

1. Introduction

Inspired by natural biological structures, cable-driven continuum robots (CDCRs) resembling elephant trunks, octopus tentacles, and snakes demonstrate the unique advantages of high compliance, super dexterity, and a large reachable workspace compared to those of traditional rigid-linked robots.[1] In general, a CDCR has a long central backbone, and it is often composed of a flexible hose with several rigid flanges spaced apart along its length.[2] These cables are routed parallel to the backbone, connected to the flanges, and activated by the motor, which generates smooth robot bending motions via the continuous elastic deformation of the backbone. Further, it can passively adapt to the encountered obstacles. CDCRs have demonstrated wide potential applications in confined and cluttered spaces such as in-space inspection and repair,[3] search and rescue, and minimally invasive surgery.[4]

There is a significant challenge in enabling CDCR perception to achieve closed-loop control.[5] In the early stage, the vision-based method was investigated for tracking continuum robots, wherein images were used to compute the bending curvature.[6] However, this method is computationally inefficient and strongly affected by light and shadow, which restricts its use in monitoring robot movements.[6] Recently, fiber Bragg grating (FBG) sensors have been applied to sense the curvature of the CDCR based on the principle that strain affects the refraction index and periodic spacing of the grating planes. However, the high modulus and extremely low fracture strain (0.4%) of the FBG sensors can significantly restrict the robot's movements; this can cause the sensors to easily rupture after a large elastic deformation of the CDCR.[7] Therefore, it remains a great challenge to develop stretchable, conformal, and self-adhesive sensors for CDCR.

Polymeric ionic hydrogels are 3D macromolecular networks containing liquid water and mobile conductive ions; they are soft, wet, and similar to biological tissues.[8] Further, polymeric ionic hydrogels can be designed to be highly stretchable[9] or as adhesive materials for various substrates.[10] Flexible hydrogel sensors have been developed based on capacitive,[11] voltage[12] or resistance[13] sensing technologies, and they can

H. Yan, G. Gao, Z. Xu, T. Chen
Key Laboratory of Marine Materials and Related Technologies
Zhejiang Key Laboratory of Marine Materials and Protective Technologies
Ningbo Institute of Materials Technology and Engineering
Chinese Academy of Sciences
Ningbo 315201, P. R. China
E-mail: gaogr@nimte.ac.cn; tao.chen@nimte.ac.cn
Y. Wang, W. Shen, F. Li, T. Zheng, S. Qian, C.-y. Chen, C. Zhang, G. Yang, T. Chen
Zhejiang Key Laboratory of Robotics and Intelligent Manufacturing Equipment Technology
Ningbo Institute of Materials Technology and Engineering
Chinese Academy of Sciences
Ningbo 315201, P. R. China
E-mail: zhengtianjiang@nimte.ac.cn; zhangchi@nimte.ac.cn
Y. Wang, W. Shen, G. Gao, T. Zheng, Z. Xu, S. Qian, C.-y. Chen, C. Zhang, G. Yang, T. Chen
School of Chemical Sciences
University of Chinese Academy of Sciences
Beijing 100049, P. R. China

The ORCID identification number(s) for the author(s) of this article can be found under https://doi.org/10.1002/adfm.202203241.

DOI: 10.1002/adfm.202203241
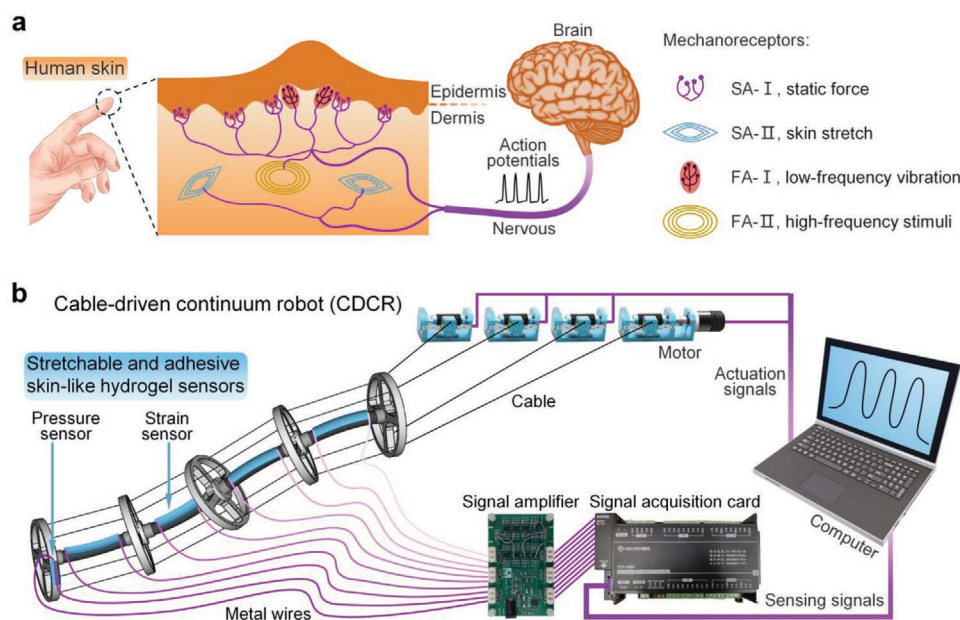
Figure 1. Cable-Driven Continuum Robot Perception Using Skin-Like Hydrogel Sensors. a) Schematic showing mechanoreceptors in the skin and the transduction of tactile signals from the human skin to the brain. b) Illustration of the sensing feedback system of a CDCR. The signal amplifier provides an independent current circuit to each sensor. Sensing signals were read and sent to the computer through a signal acquisition card. The computer commands the motors to rotate for driving the CDCR.

sense strain,[14] pressure,[15] touch position,[10a] temperature,[16] etc. Therefore, polymeric ionic hydrogels are a key candidate for CDCR sensing systems, similar to how the human skin is required for perception.

Human skin provides the ability to sense thermal and mechanical stimuli in addition to different sensations such as pain and itching (**Figure 1**a).[17] There are four types of mechanoreceptors in the skin: two slow-adapting receptors (SA-I and SA-II) that respond to sustained pressure and skin stretch, and two fast-adapting receptors (FA-I and FA-II) that can sense low- (5–50 Hz) and high-frequency vibrations (up to 400 Hz), respectively.[18] The sensed signals from the receptors are transported through nerve fibers and interpreted by the brain to provide complex information about limb bending degree, object hardness, shape, etc. In this study, we developed a new strategy to enable CDCR perception using skin-like sensors made from ionic conductive hydrogels (Figure 1b). The fabricated hydrogel contained different networks of cross-linked polyacrylamide and alginate, along with nanoclays and charge carriers Cl^- and Na^+; it exhibited an ionic conductivity of 0.91 S m^{-1}, a fracture strain of 1840%, a tensile strength of 41 kPa, and a modulus of 9.3 kPa. Through intermolecular interactions, the designed hydrogel demonstrated adhesion to many different substrate materials such as plastic, rubber, fabric, and metal, which promote the possibility of designing a CDCR with skin-like properties. The strain and pressure sensors were prepared based on the principle that the relative resistance ($\Delta R/R_0$) of a hydrogel is positively correlated with the strain during uniaxial stretching and negatively correlated with the pressure in uniaxial compression tests. Skin-like sensors are installed on the backbone and terminal flange of the CDCR (Figure 1b) to achieve proprioception to perceive its bending degrees and directions and exteroception to perceive barriers, traps, and flat roads.

A closed-loop control system is developed to precisely control the bending directions and degrees of the CDCR based on the sensing feedback from strain sensors attached to the backbone (Figure 1b). Therefore, it is confirmed that hydrogel sensors can function as human skins to enable CDCR to perform like an intelligent humanoid.

2. Results and Discussion

2.1. Structure and Properties of Polymer Ionic Hydrogels

Hydrogels consist of covalently cross-linked polyacrylamide (PAAm), ionically cross-linked alginate (Alg), nanoclays, and Na^+ and Cl^- ions (**Figure 2**a). For the synthesis of hydrogels, acrylamide and sodium alginate were dissolved in the aqueous solution of nanoclays, and N, N'-methylene-bisacrylamide (MBAA) at 0.06 wt% of acrylamide was added as cross-linker for PAAm, while $CaSO_4 \cdot 2H_2O$ was added as an ionic cross-linker for Alg. On adding NaCl, mobile Na^+ and Cl^- ions were produced, and then, ammonium peroxodisulfate was added as the initiator for PAAm; N, N, N', N'-tetramethylethylenediamine was used as the catalyst. Hydrogels were obtained after the polymerization of the solution in polyethylene terephthalate (PET) molds at 25 °C for 24 h. A small amount of MBAA was used to construct a resilient polymer network without compromising stretchability.[19] The cross-linking between Alg and Ca^{2+} was used to toughen the hydrogel, which provides an additional energy dissipation capability.[9] Nanoclays have been used to improve the modulus of hydrogels,[20] which helps avoid excessive deformation during sensor mounting. The as-prepared hydrogel showed a fracture strain of 1840%, fracture stress of 41 kPa, and modulus of 9.3 kPa (Figure S1, Supporting

Figure 2. Chemical structure and adhesion property of polymer ionic hydrogels. a) Schematic of the chemical structure of hydrogels. b) Schematic of intermolecular interactions between the hydrogel and the adherend. c) Photo showing hydrogel peeling from the CDCR backbone. d) Typical lap shear curves of hydrogels adhered to paper, cotton fabric, nitrile rubber, PET, copper foil, and PDMS. e) Adhesion strength of hydrogels adhered to various substrates. Data are means ± S.D., $n = 5$. Scale bar, 1 cm.

Information). The modulus was significantly larger than that of the hydrogel without nanoclays (2.9 kPa, Figure S1, Supporting Information). The photograph in Figure S2 (Supporting Information) shows that the hydrogel was stretched to 1400% strain.

Ionic cross-linking between Ca^{2+} and alginate was studied using Fourier transform infrared (FTIR) spectroscopy (Figure S3a, Supporting Information). Calcium alginate (Ca-Alg) was produced by mixing sodium alginate (Na-Alg) solution with $CaSO_4 \cdot 2H_2O$. The ion exchange occurs between monovalent Na^+ and divalent Ca^{2+}. Na-Alg showed peaks at 1590 cm^{-1} for asymmetric COO^- stretching, and at 1405 cm^{-1} for symmetric COO^- stretching.[9,21] These peaks shifted to 1596 and 1411 cm^{-1}, respectively, in the FTIR spectrum of Ca-Alg, which indicates the formation of ionic interactions between Ca^{2+} and carboxyl groups in the alginate.[22] Furthermore, hydrogen bonding in the polyacrylamide/alginate/nanoclay polymeric composite was evidenced by variable temperature FTIR spectra (Figure S3b, Supporting Information). The stretching peak of O−H in alginate blueshifted from 3435 to 3458 cm^{-1},[9,23] and the stretching vibration of N−H in polyacrylamide redshifted

**ADVANCED
SCIENCE NEWS**

www.advancedsciencenews.com

**ADVANCED
FUNCTIONAL
MATERIALS**

www.afm-journal.de

from 3200 to 3188 cm^{-1}[9,23,24] when the temperature increased from 20 to 100 °C. In addition, the C=O stretching in poly-acrylamide slightly blueshifted from 1663 to 1667 cm^{-1},[9,23,24] whereas the shoulder peak at 3622 cm^{-1} corresponds to O−H vibration in nanoclays became increasingly apparent;[20,24] these results indicate the dissociation of hydrogen bonds.[20,24,25]

Hydrogels adhere to many substances; the −COO^{-}, −OH, and −NH$_2$ groups in the hydrogels can form intermolecular interactions, which include electrostatic interactions, hydrogen bonds, and Van der Waals forces with many surfaces, and this leads to the adhesiveness of the hydrogels (Figure 2b).[26] As shown in Figure 2c, threadlike structures appeared when the hydrogel was peeled from the CDCR backbone, and this was made of nitrile rubber. Thread-like structures appeared in the peeling interface between the PET sheet and hydrogel with 0.01 wt.% MBAA cross-linkers during demolding (Figure S4, Supporting Information). However, they disappeared in the demolding interfaces of hydrogels with 0.06 or 0.12 wt.% MBAA, which indicates a denser cross-linking that leads to the reduced adhesive performance of the hydrogel. This can be attributed to an increase in cross-linking density reducing the length of polymer chains between cross-linking points, restricting their free movement, reducing the continuous inter-molecular interactions along polymer chains, and reducing the elongation of hydrogels. The lap shear curves (Figure 2d) indicate that shear displacements are longer than the length of the hydrogels (20 mm) for those adhered on paper, cotton fabric, nitrile rubber, PET, and copper (Cu) foil, and this indicates that the samples were stuck to and stretched by up and down adherends. Figure 2e summarizes the adhesion strength of the hydrogels adhered to paper, cotton fabric, nitrile rubber, aluminum (Al) foil, PET, glass, copper foil, and PDMS according to their strength.

The adhesion property is dominated by intermolecular interactions, the topology of the adherends, and energy dissipation in the crack zone of the hydrogels.[26] Carboxylates, hydroxyls, and amide groups in hydrogels can generate hydrogen bonds with cellulose in paper, cotton fabric, and silicon hydroxyls in glass. The carboxylates can generate ion–dipole interactions with cyano groups in nitrile rubber and metal complexes with aluminum and copper substrates.[27] Loosely cross-linked polymers easily penetrate the pores of porous materials such as paper, cotton fabric, and glass, which increases the contact area. In addition, ionic cross-linking and adsorption between polymer chains and nanoclays in hydrogels provide energy dissipation mechanisms for the adhesive faces, and therefore, additional energy is required to separate the adhesion. The combined effect resulted in the greatest adhesion strength appearing on the hydrogel/paper combinations (17.6 ± 1.4 kPa) and the adhesion strength of 6.6 ± 0.3 kPa for hydrogel/CDCR backbone adhesions (Figure 2e). The Van der Waals interactions may dominate the adhesion of the hydrogels to PDMS.[25]
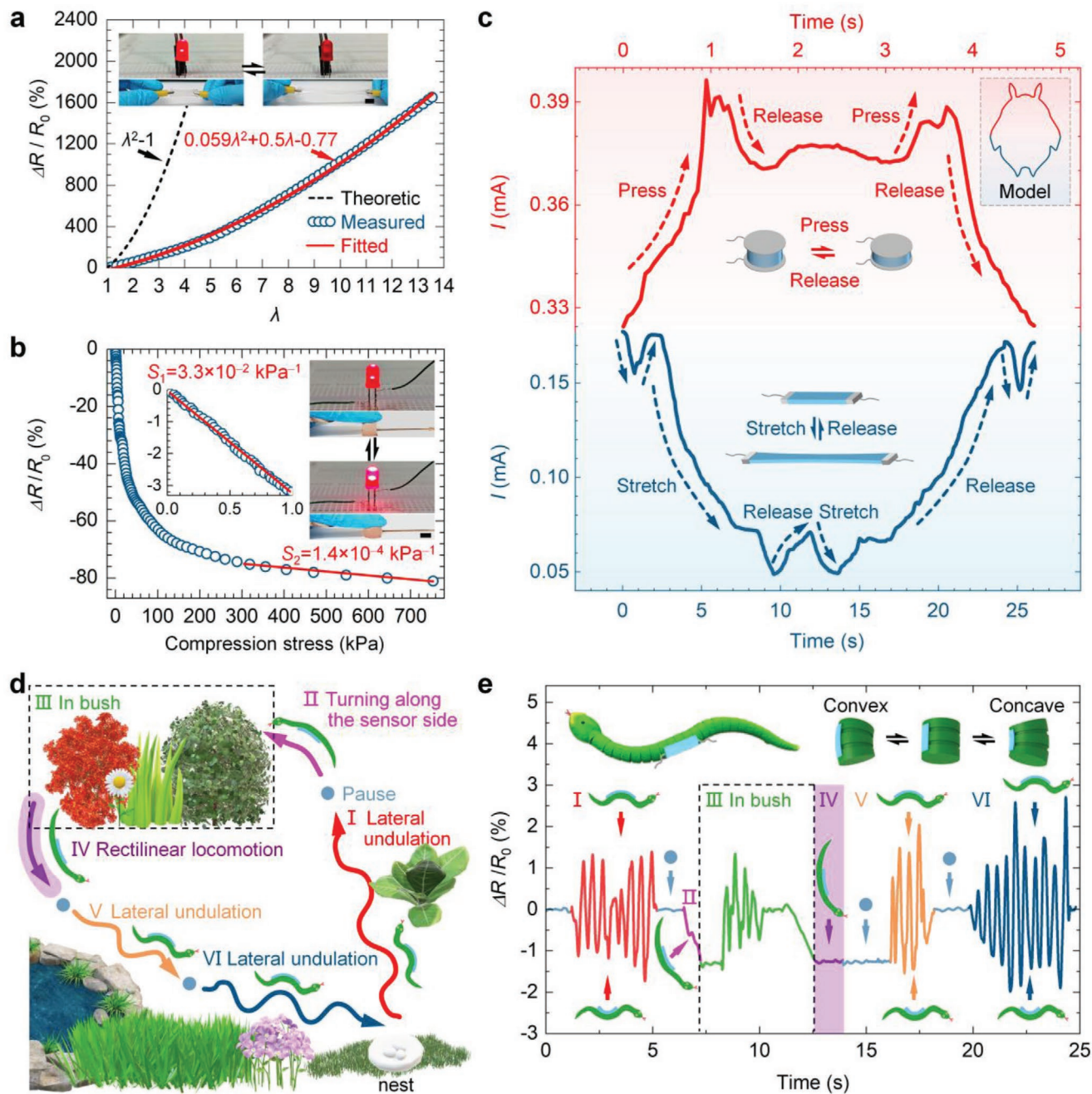
2.2. Preparation and Sensing Performance of Hydrogel Sensors

Hydrogel strain sensors were prepared based on the mechanism introduced by Keplinger et al.[8b] For a material whose conductivity (σ) is independent of the strain, resistance (R) can be calculated from $R = L/\sigma S$, where L denotes the length and S represents the cross-sectional area of the conductor. Further, it is assumed that the volume remained constant as the material deformed. The cross-sectional area scales by a factor of $1/\lambda$ when a conductor with an initial resistance R_0 is stretched to λ times its initial length; therefore, the R scale is $R = R_0\lambda^2$, and the relative resistance $\Delta R/R_0 = (R−R_0)/R_0$ scales by $\Delta R/R_0 = \lambda^2−1$. The measurement of the change in $\Delta R/R_0$ enables the conductor to sense the strain. **Figure 3**a shows that the $\Delta R/R_0$ of a hydrogel ($\sigma = 0.91$ S m^{-1}, Figure S5, Supporting Information) increased with the stretching ratio λ. As an indicator, the LED light dimmed as the hydrogel electrode in the circuit stretched from $\lambda = 1$ to 3.6. The measured $\Delta R/R_0$ versus λ curve was fitted by a quadratic function $\Delta R/R_0 = A\lambda^2 + B\lambda + C$, which results in $\Delta R/R_0 = 0.059\lambda^2 + 0.5\lambda − 0.77$; this significantly deviated from the theoretical curve $\Delta R/R_0 = \lambda^2 − 1$. A could be the strain sensitivity factor because a bigger A means a narrower parabolic opening. Further, A reduced to 0.051 when NaCl doubled and reduced to 0.025 when NaCl increased five times; this indicates that more mobile ions in the hydrogels led to lower strain sensitivity (Figure S6, Supporting Information). The A of the hydrogel sensor is considerably larger than that of the stretchable polymer/CNT composite sensor, which is 1.35×10^{-3},[28] and this indicates a higher sensitivity. The hydrogel strain sensors attached to the human forearm (Figure S7a, Supporting Information) and wrist (Figure S7b, Supporting Information) could detect the forearm twisting degree and waveform of pulse vibration. Figure S8 (Supporting Information) shows that the $\Delta R/R_0$ of a hydrogel strain sensor periodically varied from 0 to 46% because it was cyclically loading–unloading stretched from $\lambda = 1$ to 2 1000 times, which indicates that the sensor is stable and durable.

Pressure sensors were prepared based on the principle that there is a negative correlation between compression stress and $\Delta R/R_0$. Figure 3b shows the $\Delta R/R_0$ of the hydrogel in a direct-current circuit that decreased from 0 to −81.4% when the compression stress increased from 0 to 760 kPa. Correspondingly, the LED light brightened when the cylindrical hydrogel electrode was pressed to 70% of its initial height. The pressure sensitivity defined as the slope of $\Delta R/R_0$ versus the compression stress curve is 3.3×10^{-2} kPa^{-1} in the pressure range of 0–1 kPa (S_1, Figure 3b) but sharply dropped to 1.4×10^{-4} kPa^{-1} at high pressures of 300–760 kPa (S_2, Figure 3b) because $\Delta R/R_0$ changes exponentially with the compression stress.[29] The detection limit is lower than 0.1 kPa, which indicates that it is sufficiently sensitive to detect tiny forces.

We used real-time sensing signals to comprehensively demonstrate the sensitivity, stability, and reliability of the strain and pressure sensors, i.e., current (I)–time (t) curves, to draw a portrait of the cartoon character Totoro (Figure 3c). A pressure sensor is used to draw the upper body. As the pressure increased, decreased, or remained constant, the sensing curve moved upward, downward, or forward over time. A strain sensor is used to draw the lower body; stretching, releasing, or holding the sensor can lead to a downward, upward, or forward movement of the I–t curve. As shown in Figure 3c and Movie S1 (Supporting Information), the ears, limbs, and fat body of the portrait matched the model well.

Figure 3. Sensing performance of hydrogel strain and pressure sensors. a) Theoretic, measured, and fitted curves of $\Delta R/R_0$ of a strain sensor varied by the stretching ratio (λ). Inserted photos show an LED light dimmed as a hydrogel electrode was stretched. b) $\Delta R/R_0$ and sensitivity (S) varied by the compression stress of a pressure sensor. The inserted curve shows the details at stress below 1 kPa. Inserted photos show an LED light brightened as a hydrogel electrode was pressed. c) A portrait comprising two I–t curves, whose shapes were controlled by manually operating the pressure (upper) and strain (lower) sensors. d) A roadmap for a trip of a snake robot. e) $\Delta R/R_0$ of a strain sensor varied by time in the trip. Inserted schemes show the sensor deformed by snake bending: scale bars, 1 cm.

We chose a snake robot to prove the concept of monitoring movements using the adhesive sensor, especially in the invisible space (Figure 3d). A snake robot comprises many cylindrical segments (Figure 3e) and imitates two modes of snake locomotion: lateral undulation and rectilinear locomotion.[30] During lateral undulation, alternating left and right bends propagate from the front to the rear of the body, which helps generate propulsive forces. In rectilinear locomotion, a snake uses the movements of the belly skin to propel the body while its ribs are immobile; the body does not need to be straight in this mode. A strain sensor was mounted on the lateral side of the snake's body (Figure 3e), and the sensor was stretched on the convex side; however, it compressed on the concave side during lateral undulation.

**ADVANCED
SCIENCE NEWS**

www.advancedsciencenews.com

**ADVANCED
FUNCTIONAL
MATERIALS**

www.afm-journal.de

We recorded the sensing signals (Figure 3e) on a trip of the snake (Figure 3d; Movie S2, Supporting Information); it left the nest and moved forward by lateral undulation (Figure 3e, I) until it paused in the front of the bush. Then, it moved into the bush by turning along the sensor side (II). Movements in the bush are unobservable (III); after a moment, it came out by rectilinear locomotion (no swing of the body, IV). Next, it alternatively pauses and laterally undulates (V and VI) until it returns to the nest. In steps I, V, and VI, the sensing signals ($\Delta R/R_0$) oscillate around zero over time; in step II, $\Delta R/R_0$ decreases slowly over time. In step IV, $\Delta R/R_0$ did not change over time. The changes in $\Delta R/R_0$ in Figure 3e matched well with the locomotion in Figure 3d. Therefore, one can speculate the movements of the snake in the bush according to $\Delta R/R_0$ changes (Figure 3e); after a pause ($\Delta R/R_0$ was constant), it moved by lateral undulation ($\Delta R/R_0$ oscillated), followed by another pause ($\Delta R/R_0$ was constant), and then it turned along the sensor side ($\Delta R/R_0$ slowly decreased). The "pause" may be "rectilinear motion," as both did not result in noticeable $\Delta R/R_0$ changes.

2.3. Detecting Bending Degrees and Directions

Strain sensors were used to detect the bending degree of the CDCR. The backbone of the CDCR is a rubber hose separated into several connected segments using rigid supports (**Figure 4**a). The flange is fixed to each support (Figure 4c), and a strain sensor is attached to each of the top three segments (Figure 4a). The hydrogels are elongated or shortened by CDCR bending. As illustrated in Figure 4b, a segment with an axis length of γ and diameter Φ is bent into a semicircle. Assuming that the axis length is constant during bending, the sensor with the initial length x is stretched to $(1 + \pi\Phi/2\gamma)x$ on the convex side and shortened to $(1 - \pi\Phi/2\gamma)x$ on the concave side of the segment (Figure 4b). Therefore, the strain sensors can be used to measure the bending degrees (θ, Figure 4a). For example, $\Delta R/R_0$ of the three sensors increases from 0 to 1.9% when the three segments are bent to the left synchronously with $\theta = 4.5°$ (Figure 4c, I,d, I). The $\Delta R/R_0$ of the upper sensors changed to 2.2% and the lower one changed to 4.3% when the upper two segments bent to 6.1° and the lower one bent to 11.6° (Figure 4c, II,d, II). Further, $\Delta R/R_0$ increased to 3.3%, 3.3%, and 6.3% as these segments bent to 8.9°, 8.9°, and 21.6°, respectively (Figure 4c, III,d, III). In addition, $\Delta R/R_0$ decreased from 0 to the negatives when the segments bent to the right, and the changes of $\Delta R/R_0$ were proportional to θ in repeated bending–unbending cycles (step IV–VI, Movie S3, Supporting Information).

These two strain sensors can detect the bending direction of a segment. In Figure 4e, six strain sensors are mounted on two adjacent segments. They are located on the left (1#), front (2#), and right (3#) side of the upper segment, and the left (4#), front (5#), and right (6#) surfaces of the lower segment (Figure 4e). The third sensor in each segment provides an additional basis for determination. A customized signal amplifier (Figure S9a, Supporting Information) provides an independent current to each sensor and converts the resistance changes of the sensors into voltage signals. An increase in $\Delta R/R_0$ corresponds to a decrease in $\Delta V/V_0$ (Figure S9b, Supporting Information). Initially, the backbone
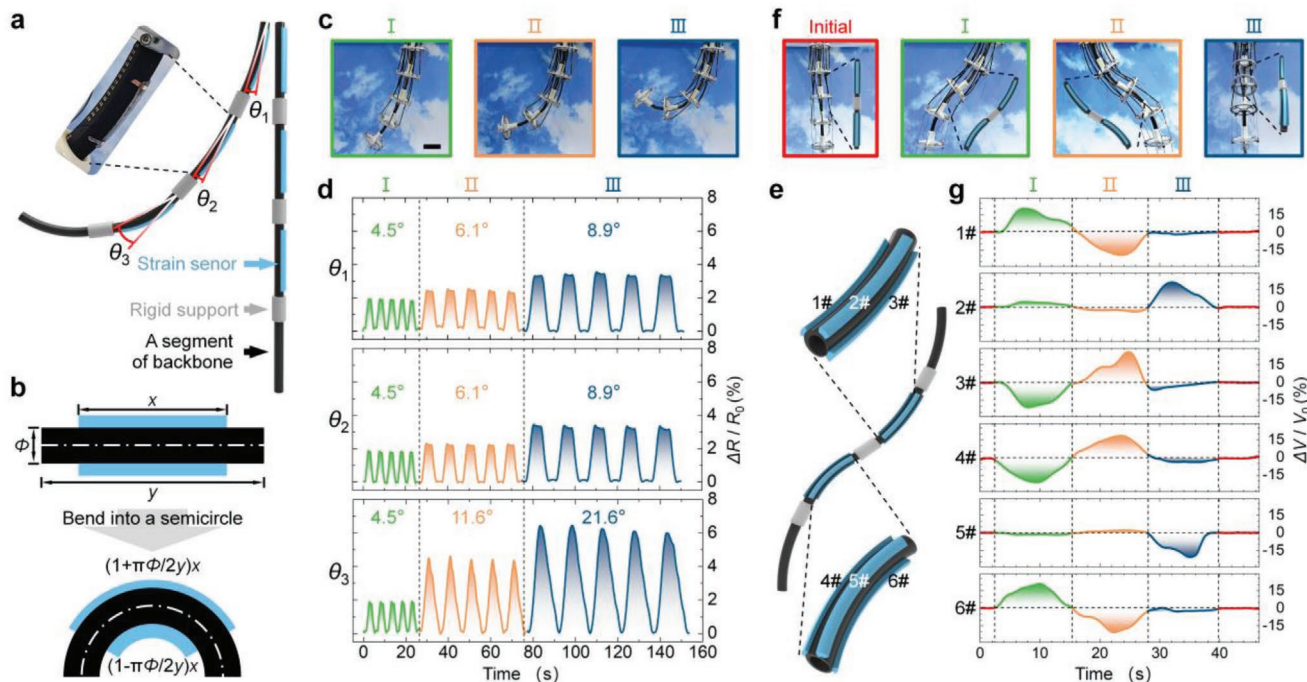
Figure 4. Detecting bending degrees and directions of CDCR. a) Schematic and photo show strain sensors adhered on a CDCR backbone and the definition of bending degree (θ). b) A schematic illustrates the length of the two strain sensors changed by CDCR bending. c) Photos indicate the CDCR bent to various degrees. d) Corresponding sensing signals. e) A schematic shows six strain sensors on two adjacent backbone segments for detecting bending directions. f) Photos of the CDCR bent in different directions. g) Corresponding sensing signals. Scale bar, 10 cm.

is perpendicular to the ground (Figure 4f, initial), and the $\Delta V/V_0$ of all sensors is 0 (Figure 4g). In step I (Figure 4f), the upper segment bends to the left and the lower segment bends to the right synchronously; then, they both turn back. Sensors 1# and 6# were shortened, sensors 3# and 4# were elongated, and the lengths of sensors 2# and 5# were not theoretically changed in the cycle. Correspondingly, the $\Delta V/V_0$ of sensors 1# and 6# increased to crests at 20%; then, they decreased to 0. The $\Delta V/V_0$ of sensors 3# and 4# decreased to troughs at −21% and returned to 0, while sensors 2# and 5# showed negligible $\Delta V/V_0$ changes (Figure 4g). According to the former example, one can easily conclude from step II of Figure 4g that the upper segment is bent to the right; in contrast, the lower segment bent to the left because there were remarkable troughs in the $\Delta V/V_0$ curves of sensors 1# and 6#, and distinctive crests in sensors 3# and 4#, whereas no noticeable $\Delta V/V_0$ changes occurred for sensors 2# and 5#. As shown in step III in Figure 4g, a crest appeared in curve 2#, a trough appeared in curve 5#, and there were almost no changes for the other curves, which indicates that the upper segment bent forward and lower one bent backward. These results were verified in Figure 4f and Movie S4 (Supporting Information).

2.4. CDCR Perceiving Surrounding Spaces

Strain and pressure sensors were employed to help the CDCR perceive surrounding spaces, avoid obstacles, and explore the way. Seven sensors are adhered to the CDCR, which includes strain sensors 1#, 2#, 3#, and 4# on four backbone segments, and pressure sensors 5#, 6#, and 7# on the rim of the terminal flange (**Figure 5**a). A vacuum nozzle is mounted at the end of the CDCR to absorb the objects (Figure 5a). A mountain is located in front of the CDCR; there is a pool, an apple tree, peaks on the top, and a cave at the bottom right of the mountain (Figure 5b,c). In the initial stage, the CDCR is vertical, and $\Delta V/V_0$ is 0 for all sensors.

The CDCR performs subsequent actions (Figure 5c; Movie S5, Supporting Information) based on the sensing signals (Figure 5d); it is first bent to the right and left sides. $\Delta V/V_0$ for sensors 5#, 6#, and 7# is 0 (Figure 5d, before I), which indicates the absence of obstacles. Next, it bent forward. The rising in curves 1# and 2# (Figure 5d, I) exhibits forward bending of the segments, whereas a wave crest appears in curve 5# (Figure 5d, I), which indicates that there is an obstacle (Figure 5c, I). Subsequently, the robot moved along the obstacle. Curve 5# changes to 0 (Figure 5d, II) because of the cave (Figure 5c, II); it turns back and moves to the left along the obstacle until it reaches the edge (Figure 5c, III), as evidenced by the plateau signal in curve 5# (Figure 5d, III). Thus, we turned to exploring the top. The rising in curves 3# and 4# (Figure 5d, between III and IV) indicate the bending of the segments. The $\Delta V/V_0$ of curve 6# increased from 0 (Figure 5d, IV), and it suggests that the final flange landed on the top (Figure 5c, IV). Subsequently, it was moved to the right. Curve 6# is changed to 0 (Figure 5d, V), and therefore, it bends the final segment to probe down (Figure 5d, V, 4# and Figure 5c, V). However, the $\Delta V/V_0$ of curve 6# is always 0 (Figure 5d, V), and it keeps moving to the right. After a

moment, a plateau appears in curve 6# (Figure 5d, VI), which indicates that the final flange crossed a trap. A sharp peak appears in curve 7# (Figure 5d, VI), which suggests that it hits a hard barrier (Figure 5c, VI). Therefore, it turned back. When it reaches the trap again, it raises the final flange to crossover (Figure 5d, VII, 3#). At this moment, the vacuum nozzle sucks an apple (Figure 5c, VII). The apple is pulled down, it lands on the mountain (Figure 5d, VIII, 6#, and Figure 5c, VIII), returns, and it is finally recovered vertically. In this discovery trip, the $\Delta V/V_0$ curves of the seven sensors precisely record the actions of the CDCR, as shown in Figure 5c and Movie S5 (Supporting Information). These sensors can be used as the bionic skins for soft robots.

2.5. Closed-Loop Control

We develop a closed-loop system to control the bending degree and direction of the CDCR (**Figure 6**a). It comprises a sensing and driving system and a computer (Figure 6a). In the sensing part, two strain sensors were adhered on the two sides of a backbone segment and connected to a signal amplifier, signal acquisition card, and computer in sequence. The amplifier provides an independent current for each hydrogel sensor; the amplified voltage signals (V_1 and V_2) were inversely proportional (Figure S9b, Supporting Information) to the resistance of the left (R_1) and right sensor (R_2), respectively. V_1 and V_2 are recorded over time; the two motors are connected to the same motion controller and computer sequentially in the driving part. The computer controls the bending based on the sensing signals using a closed-loop algorithm (Figure 6b). Three parameters (c_0, c^*, and c_t) were defined; c_0 is equal to V_2-V_1 when the segment is straight, c^* represents a set value, i.e., the target value of V_2-V_1, where c_t represents the measured V_2-V_1, which varies with time. The algorithm comprises four steps (Figure 6b): I, set a c^*; II, get a c_t; III, calculate the angular offset $\Delta\theta = \alpha(c^*-c_t)$, where α represents the bending factor; and IV, the CDCR segment bends $\Delta\theta$ to bring c_t close to c^*. Steps II–IV were cycled spontaneously. After the program runs, the CDCR segment bends toward the set bending degree, and then, it oscillates slightly near the set degree.

c^* can be used as a parameter to determine the bending degree and direction. Initially, the CDCR segment is straight (Figure 6a; Figure S10a, Supporting Information), with a c_0 of 2.15 V (Figure S10a,b, Supporting Information). If it bent to the left (Figure 6c), the left sensor would be shortened, and the right one elongated (Figure 4b); thereby, R_1 decreased, R_2 increased, V_1 increased, and V_2 decreased, which leads to $c_t < c_0$. Therefore, a c^* value less than c_0 leads to left bending, and the bending degree is proportional to c_0-c^*. Otherwise, a c^* larger than c_0 results in a right bending. We set the c^* value to 2 V, as shown in Figure 6c; the segment bent to the left with an average c_t of 2 ± 0.05 V. The CDCR was controlled to maintain an average bending degree of −0.86 ± 0.04 rad in 1 min, with the degree oscillated in the range of −0.95 – 0.8 rad (Figure 6d; Movie S6, Supporting Information). Next, we set a c^* of 2.3 V. The segment bent to the right (Figure 6e) with an average c_t of 2.3 ± 0.04 V; it is controlled to maintain an average bending
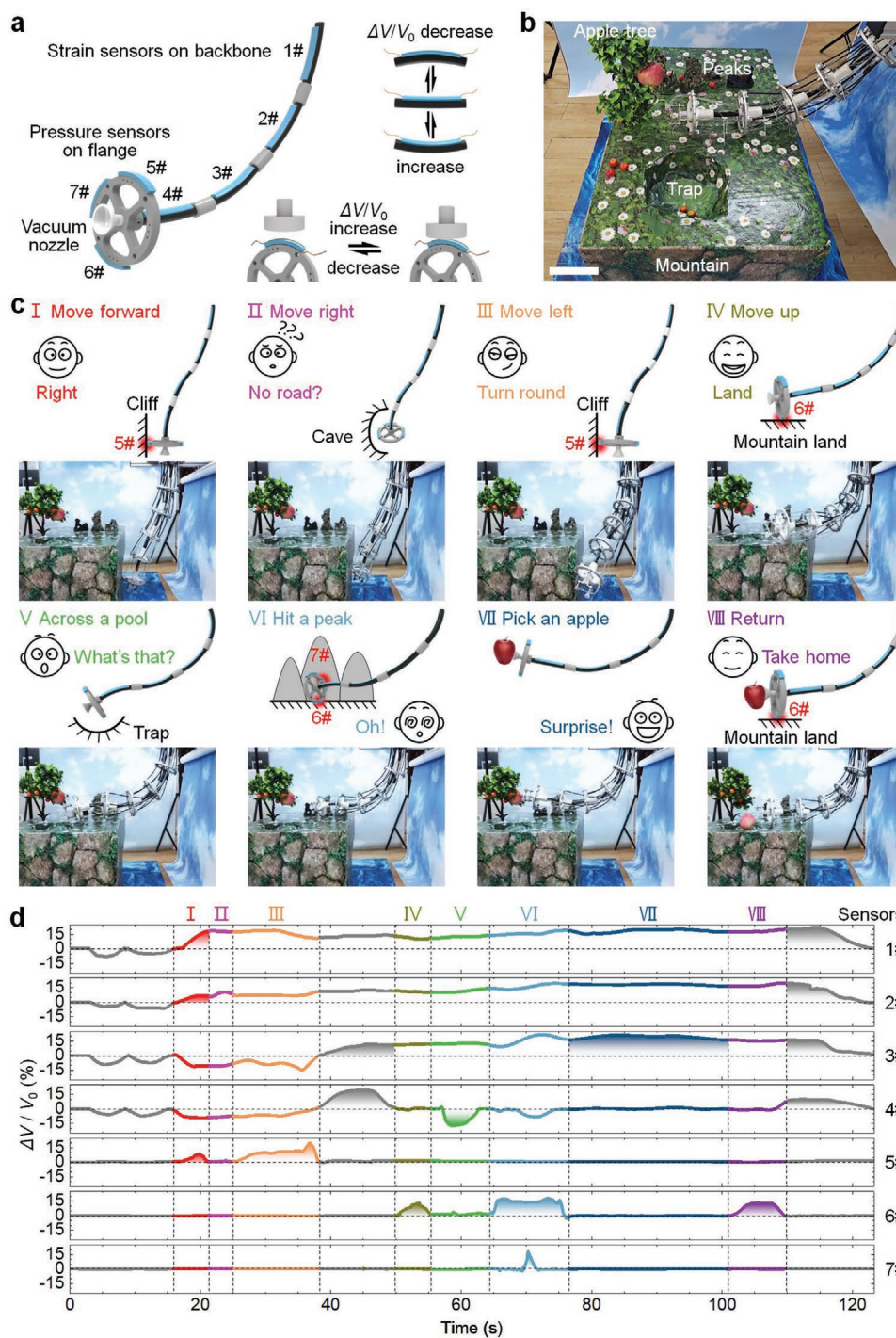
Figure 5. CDCR perceiving surrounding spaces. a) Schematics show sensors on CDCR, and voltage signal changes by bending and pressing sensors. b) photo showing the scenario around the CDCR. c) Photos recorded the movements of CDCR. The schematic on the top of each photo illustrates the encounter and shape of the robot. d) $\Delta V/V_0$ of seven sensors varied by time as the CDCR explored the neighboring spaces. Scale bar, 20 cm.

degree of 0.51 ± 0.03 rad in 1 min, with the degree slightly oscillated in the range of $0.45 - 0.56$ rad (Figure 6f; Movie S6, Supporting Information). We use $V_2 - V_1$, rather than a signal from only one hydrogel sensor, as a parameter to control CDCR bending. The application of the two hydrogel sensors is beneficial for the accurate and stable control of the bending degree of CDCR; the resistances of hydrogels are prone to fluctuations caused by changes in temperature,[8a,11,16] humidity,[31] and light intensity.[31c,32] Although the difference between the two sensing signals $(V_2 - V_1)$ is relatively insensitive to these factors, V_1 and V_2 curves always rose and fell in sync in Figure 6d,f, respectively.
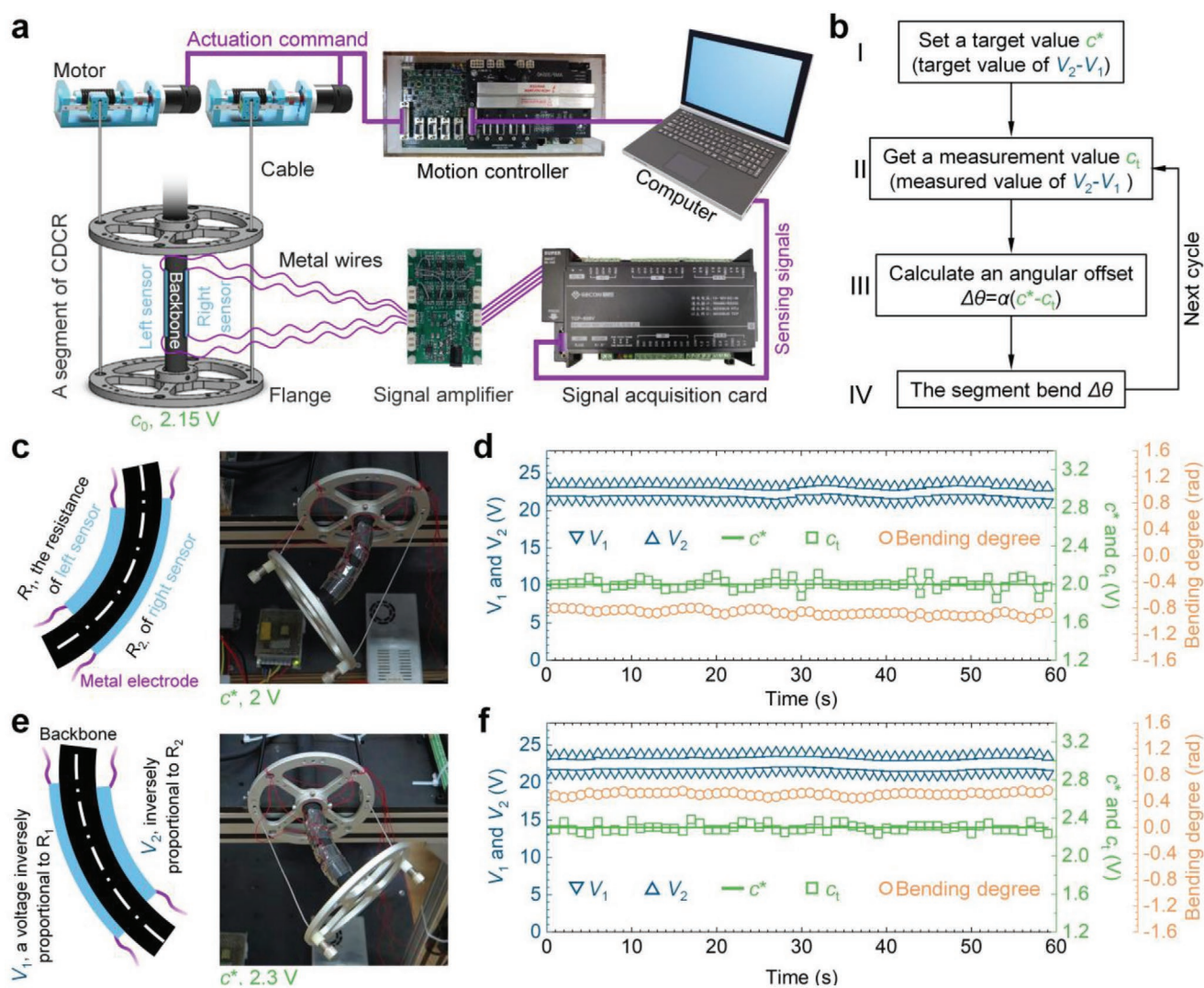
Figure 6. Closed-loop control. a) A detailed circuit diagram of the closed-loop control system. b) Block diagram illustrates the logic of closed-loop control. c) Schematic diagram (left) and photo (right) show the CDCR segment and sensors bent to the left. d) Corresponding V_1, V_2, c^*, c_t, and bending degree varied by time. e) Schematic (left) and photo (right) show them bent to the right. f) Corresponding parameters varied by time.

3. Conclusion

We reported a skin-like sensing strategy based on stretchable, conformal, and adhesive hydrogel sensors to enable CDCR proprioception, exteroception, and closed-loop control. We fabricated strain and pressure sensors according to the principle that the electrical resistances of ionic conductive polyacrylamide/alginate/nanoclay polymeric composite hydrogels are positively correlated with strain and negatively correlated with pressure. Hydrogel sensors have several advantages over the commonly used FBG sensors, which includes ultrahigh stretchability (1840%), ultralow modulus (9.3 kPa), and ability to adhere to the backbone and flange of the CDCR. We drew a portrait using the current–time curves as painting lines, whose shape was manually controlled by stretching–releasing and pressing–releasing sensors, to illustrate the sensitivity, stability, and reliability of the sensors. We demonstrated the monitoring of the locomotion of a snake robot in an out-of-sight space

using a strain sensor. We demonstrated that the CDCR could perceive its bending degree and direction, barrier, trap, and flat road with the help of the hydrogel sensors. We developed a closed-loop system to actively control the bending of a CDCR and maintain its bending degree near the target degree. Our work illustrated that the stretchable and adhesive hydrogel sensors could work like human skin to enable CDCR perception and are promising for use in the development of soft robotics that performs like intelligent humanoids.

4. Experimental Section

Materials: Sodium alginate (Na-Alg), N, N'-methylene-bisacrylamide (MBAA), ammonium persulfate (APS), and N, N, N', N'-tetramethylethylenediamine (TEMED) were purchased from Shanghai Aladdin Biochemical Technology Co., Ltd. Acrylamide (AAm), NaCl, $CaSO_4 \cdot 2H_2O$, and rhodamine B were purchased from Sinopharm Chemical Reagent Co. Ltd. Synthetic nanoclays (formula:

$Mg_{5.34}Li_{0.66}Si_8O_{20}(OH)_4Na_{0.66}$, molecular weight: 762.3 g mol^{-1}, trademark: Laponite XLG) was purchased from BYK Additives & Instruments, Co., Ltd. VHB 4905 elastomer tapes were obtained from 3 M Corporation. Deionized water was used in all experiments.

Preparation of Hydrogels: Nanoclays (0.15 g, 0.2 mmol) were dispersed in water (13 ml) and stirred overnight. Then, Na-Alg (0.15 g) was added, and it was followed by stirring for 12 h. Next, AAm (1.8 g, 25 mmol), MBAA (1.08 × 10^{-3} g, 0.06 wt.% to AAm), CaSO$_4$·2H$_2$O (3.12 × 10^{-4} g, 0.21 wt.% to Na-Alg), and NaCl (0.15 g, 2.6 mmol) were added and stirred for 2 h at ice-water temperature. Then, APS (1.8 × 10^{-2} g, 1 wt.% to AAm) and TEMED (10 μl) were added, and the mixture was stirred for 10 min. The final solution was poured into a flat chamber composed of two polyethylene terephthalate (PET) sheets separated by a silicone gasket. Polymerization was conducted at room temperature for 24 h.

FTIR Measurements: The FTIR spectra of sodium alginate (Na-Alg), calcium alginate (Ca-Alg), and freeze-dried hydrogels were recorded on a Thermo Scientific Nicolet 6700 FTIR spectrometer. Temperature-varied FTIR spectra were recorded using the same spectrometer equipped with a temperature control module. A mixed solution containing CaSO$_4$·2H$_2$O (3.12 × 10^{-4} g), Na-Alg (0.15 g), and water (10 mL) was ultrasonically dispersed for 30 min, stirred for 10 h, and freeze-dried to prepare Ca-Alg.

Lap Shear Tests: A piece of hydrogel (20 mm × 20 mm × 2 mm) was attached to two rectangular adherends (20 mm wide and 60 mm long). An assembly with a sandwich structure in the middle (Figure 2d) was mounted on a universal testing machine (Zwick/Roell Z1.0) and stretched at 100 mm min^{-1} until separation. The adhesion strength was determined by dividing the maximum force (F_{max}) by the bonded area (400 mm^2), F_{max}/400 mm^2. Polyimide films such as PDMS and nitrile rubber were bonded to elastomer adherends.

Preparation of Hydrogel Sensors: A strain sensor was prepared by attaching copper wire electrodes to the two ends of a hydrogel strip, and it was then connected to a circuit. A pressure sensor was designed by attaching copper wire electrodes to the upper and lower surfaces of the hydrogel block and then connected to a circuit. The sensors were covered with VHB 4905 elastomer tape to prevent water evaporation when subjected to the stability test and attached to the robots. The copper wires were firmly fixed between the tape and hydrogel surfaces. The volunteer shown in Figure S7 (Supporting Information) for motion measurement and pulse detection provided informed written consent to wear the sensor.

Mechanical Tests: Mechanical tests were conducted at room temperature using a universal testing machine (Zwick/Roell Z1.0) equipped with a 1 kN load cell. Tensile tests were performed on hydrogel strips (30 mm × 10 mm × 2 mm) with a cross-head distance of 10 mm and a constant tensile speed of 100 mm min^{-1}. The tensile strain (ε) was calculated from $\varepsilon = (l-l_0)/l_0 × 100\%$, where l represents the length and l_0 represents the initial length of the sample. The stretch ratio (λ) is calculated as $\lambda = l/l_0$. The tensile stress was equal to F/A_0, where F represents the force and A_0 represents the initial cross-sectional area of the sample.

Compression tests were performed on cylindrical pressure sensors (15 mm in diameter and 20 mm in height) at a compression speed of 10 mm min^{-1}. Compression stress was defined as F/A_0.

Conductivity Measurement: Conductivity was measured by electrochemical impedance spectroscopy using an electrochemical workstation (CHI660E, Shanghai Chenhua Instrument Co., Ltd.). The hydrogel sample (30 mm × 10 mm × 2 mm) was sandwiched between two copper electrodes (30 mm in length and 10 mm in width); the test frequency varied from 0.01 to 1 × 10^5 Hz and the amplitude was 5 mV. The intercept of the real part of the Nyquist plot was taken as the resistance (R) of the hydrogel. The conductivity (σ) was calculated from $\sigma = d/RA$, where d and A represent the distance between the electrodes and area of the electrode, respectively.

Current–Time (I–t) Curve Measurement: An electrochemical workstation (CHI660E) was used to record the direct current (I) in the hydrogel sensor, which varied with time (t). A multichannel electrochemical workstation (Solartron 1470e, Solartron Enterprises) was used to record the I–t curves from multiple hydrogel sensors synchronously. A constant voltage of 0.1 V was applied in all tests.

Relative Resistance–Time ($\Delta R/R_0$–t) Curve Measurement: The relative resistance ($\Delta R/R_0$) change of a sensor was calculated from the formula $\Delta R/R_0 = (R-R_0)/R_0 = I_0/I-1$, where R_0 and I_0 represent the initial resistance and initial current, respectively.

Relative Voltage–Time ($\Delta V/V_0$–t) Curve Measurement: A customized signal amplifier was employed to convert the resistance of the hydrogels into voltage signals. An increase in $\Delta R/R_0$ led to a decrease in $\Delta V/V_0$; the detailed signal conversion mechanism is shown in Figure S9 (Supporting Information).

Closed-Loop Control: Two hydrogel strain sensors (60 mm × 10 mm × 2 mm) adhered to the left and right sides of a CDCR segment were covered with VHB 4905 films to prevent the evaporation of water. The signal amplifier provided an independent current for each sensor. The resistances of the left (R_1) and right (R_2) hydrogels were converted into voltage signals recognized by the signal acquisition card (GECON TCP-508 V, Fuzhou GECON Electronics Co., LTD). The computer recorded voltage signals corresponding to the left (V_1) and right (V_2) sensors and calculated c_t (=V_2-V_1). The computer calculated the angular offset $\Delta\theta$ (=$\alpha(c^*-c_t)$), commanding the motion controller (AMP-20540, Galil Motion Control, Inc.) to regulate the rotation of the motors when c^* was input, which led to the segment bent $\Delta\theta$. The bending factor α was an empirical value (0.48 rad V^{-1}). A larger α led to larger oscillation amplitudes, and a smaller α led to more bending steps being required to approach the set bending degree. The computer measured the real-time bending degree (rad) of the CDCR segment according to the change in the length of the left and right cables. The relationship between the CDCR bending degree and lengths of the two cables was precalibrated.

Statistical Analysis: The adhesion strength data in Figure 2e are presented as mean ± standard deviation calculated for the five independent samples using Microsoft Excel (2019). The average c_t and bending degrees in the closed-loop control were presented as the mean ± standard deviation calculated for 60 consecutive data points in 1 min. The polynomial fitting curve in Figure 3a and the linear fitting curve in Figure 3b are analyzed using the ORIGIN (2021) software. The relative voltage $\Delta V/V_0$ was transformed from the real-time voltage V and initial voltage V_0 using the formula $\Delta V/V_0 = (V-V_0)/V_0$ using ORIGIN (2021).

Supporting Information

Supporting Information is available from the Wiley Online Library or from the author.

Acknowledgements

Conflict of Interest

The authors declare no conflict of interest.

Data Availability Statement

The data that support the findings of this study are available from the corresponding author upon reasonable request.

[1] a) Z. Zhang, J. Dequidt, J. Back, H. Liu, C. Duriez, *IEEE Robot. Autom. Lett.* **2019**, *4*, 1852; b) H. Yuan, L. Zhou, W. Xu, *Mech. Mach. Theory* **2019**, *135*, 130.

[2] a) C. Li, C. D. Rahn, *J. Mech. Des.* **2002**, *124*, 265; b) W. Shen, G. Yang, T. Zheng, Y. Wang, K. Yang, Z. Fang, *IEEE Access* **2020**, *8*, 37474.

[3] M. M. Tonapi, I. S. Godage, A. M. Vijaykumar, I. D. Walker, *Adv. Rob.* **2015**, *29*, 861.

[4] F. Qi, F. Ju, D. Bai, Y. Wang, B. Chen, *Int. J. Med. Rob. Comput. Assisted Surg.* **2018**, *14*, e1932.

[5] a) X. Liang, G. He, T. Su, W. Wang, C. Huang, Q. Zhao, Z. G. Hou, *IEEE Trans. Hum.-Mach. Syst.* **2022**, *52*, 26; b) D. Rus, M. T. Tolley, *Nature* **2015**, *521*, 467.

[6] M. W. Hannan, I. D. Walker, *Robotica* **2005**, *23*, 645.

[7] a) J. C. Vieira, O. M. F. Morais, C. M. A. Vasques, R. de Oliveira, *Measurement* **2015**, *61*, 58; b) R. Xu, A. Yurkewich, R. V. Patel, *IEEE Robot. Autom. Lett.* **2016**, *1*, 1052; c) S. Sefati, C. Gao, I. Iordachita, R. H. Taylor, M. Armand, *IEEE Sens. J.* **2021**, *21*, 3066.

[8] a) C.-G. Han, X. Qian, Q. Li, B. Deng, Y. Zhu, Z. Han, W. Zhang, W. Wang, S.-P. Feng, G. Chen, W. Liu, *Science* **2020**, *368*, 1091; b) C. Keplinger, J.-Y. Sun, C. C. Foo, P. Rothemund, G. M. Whitesides, Z. Suo, *Science* **2013**, *341*, 984; c) S. Wu, H. Shi, W. Lu, S. Wei, H. Shang, H. Liu, M. Si, X. Le, G. Yin, P. Theato, T. Chen, *Angew. Chem., Int. Ed.* **2021**, *60*, 21890.

[9] J.-Y. Sun, X. Zhao, W. R. K. Illeperuma, O. Chaudhuri, K. H. Oh, D. J. Mooney, J. J. Vlassak, Z. Suo, *Nature* **2012**, *489*, 133.

[10] a) G. Gao, F. Yang, F. Zhou, J. He, W. Lu, P. Xiao, H. Yan, C. Pan, T. Chen, Z. L. Wang, *Adv. Mater.* **2020**, *32*, 2004290; b) F. Ni, P. Xiao, C. Zhang, W. Zhou, D. Liu, S.-W. Kuo, T. Chen, *Adv. Mater.* **2021**, *33*, 2103937; c) H. Yuk, C. E. Varela, C. S. Nabzdyk, X. Mao, R. F. Padera, E. T. Roche, X. Zhao, *Nature* **2019**, *575*, 169.

[11] I. You, D. G. Mackanic, N. Matsuhisa, J. Kang, J. Kwon, L. Beker, J. Mun, W. Suh, T. Y. Kim, J. B.-H. Tok, Z. Bao, U. Jeong, *Science* **2020**, *370*, 961.

[12] Z. Xu, F. Zhou, H. Yan, G. Gao, H. Li, R. Li, T. Chen, *Nano Energy* **2021**, *90*, 106614.

[13] Z. Yu, P. Wu, *Adv. Mater.* **2021**, *33*, 2008479.

[14] a) J. Wei, Y. Zheng, T. Chen, *Mater. Horiz* **2021**, *8*, 2761; b) H. Li, Y. Liang, G. Gao, S. Wei, Y. Jian, X. Le, W. Lu, Q. Liu, J. Zhang, T. Chen, *Chem. Eng. J.* **2021**, *415*, 128988.

[15] a) H. Li, G. Gao, Z. Xu, D. Tang, T. Chen, *Macromol. Rapid Commun.* **2021**, *42*, 2100480; b) J.-Y. Sun, C. Keplinger, G. M. Whitesides, Z. Suo, *Adv. Mater.* **2014**, *26*, 7608.

[16] C. Zhang, Y. Zhou, H. Han, H. Zheng, W. Xu, Z. Wang, *ACS Nano* **2021**, *15*, 1785.

[17] A. Zimmerman, L. Bai, D. D. Ginty, *Science* **2014**, *346*, 950.

[18] a) R. S. Dahiya, G. Metta, M. Valle, G. Sandini, *IEEE Trans. Robot.* **2010**, *26*, 1; b) A. Chortos, J. Liu, Z. Bao, *Nat. Mater.* **2016**, *15*, 937; c) W. Zhou, P. Xiao, Y. Liang, Q. Wang, D. Liu, Q. Yang, J. Chen, Y. Nie, S.-W. Kuo, T. Chen, *Adv. Funct. Mater.* **2021**, *31*, 2105323.

[19] C.-C. Kim, H.-H. Lee, K. H. Oh, J.-Y. Sun, *Science* **2016**, *353*, 682.

[20] G. Gao, G. Du, Y. Sun, J. Fu, *ACS Appl. Mater. Interfaces* **2015**, *7*, 5029.

[21] G. Lawrie, I. Keen, B. Drew, A. Chandler-Temple, L. Rintoul, P. Fredericks, L. Grøndahl, *Biomacromolecules* **2007**, *8*, 2533.

[22] C. Sartori, D. S. Finch, B. Ralph, K. Gilding, *Polymer* **1997**, *38*, 43.

[23] Q. Zheng, L. Zhao, J. Wang, S. Wang, Y. Liu, X. Liu, *Colloids Surf., A* **2020**, *589*, 124402.

[24] Y. Deng, J. B. Dixon, G. N. White, R. H. Loeppert, A. S. R. Juo, *Colloids Surf., A* **2006**, *281*, 82.

[25] H. Shi, S. Wu, M. Si, S. Wei, G. Lin, H. Liu, W. Xie, W. Lu, T. Chen, *Adv. Mater.* **2021**, *33*, 2107452.

[26] J. Yang, R. Bai, B. Chen, Z. Suo, *Adv. Funct. Mater.* **2020**, *30*, 1901693.

[27] Y. Wang, F. Huang, X. Chen, X.-W. Wang, W.-B. Zhang, J. Peng, J. Li, M. Zhai, *Chem. Mater.* **2018**, *30*, 4289.

[28] G. Cai, J. Wang, K. Qian, J. Chen, S. Li, P. S. Lee, *Adv. Sci.* **2017**, *4*, 1600190.

[29] a) G. Ge, Y. Zhang, J. Shao, W. Wang, W. Si, W. Huang, X. Dong, *Adv. Funct. Mater.* **2018**, *28*, 1802576; b) S. Zhuo, C. Song, Q. Rong, T. Zhao, M. Liu, *Nat. Commun.* **2022**, *13*, 1743.

[30] a) B. C. Jayne, *Integr. Comp. Biol.* **2020**, *60*, 156; b) D. L. Hu, J. Nirody, T. Scott, M. J. Shelley, *Proc. Natl. Acad. Sci. U.S.A.* **2009**, *106*, 10081.

[31] a) M. B. Sobhanimatin, S. Pourmahdian, M. M. Tehranchi, *Mater. Today Commun.* **2021**, *26*, 101997; b) H. Luo, L. Liang, X. Ma, N. Liu, S. Huang, H. Sun, *IEEE Sens. J.* **2018**, *18*, 8022; c) M. Ju, B. Wu, S. Sun, P. Wu, *Adv. Funct. Mater.* **2020**, *30*, 1910387.

[32] A. Ehrenhofer, M. Elstner, T. Wallmersperger, *Sens. Actuators, B* **2018**, *255*, 1343.